Pergamon

Int. J. Rock Mech. Min. Sci. Vol. 34, No. 7, pp. 1075–1089, 1997

Printed in Great Britain
PII: S0148-9062(97)00297-0
0148-9062/97 $17.00 + 0.00

A Viscoplastic Discontinuum Model of Time-dependent Fracture and Seismicity Effects in Brittle Rock

J. A. L. NAPIER†
D. F. MALAN†

A model is proposed for the direct mechanistic simulation of seismic activity and stress transfer effects in deep level mines. The model uses a discontinuum viscoplastic formulation to relate the rate of slip on a crack to the shear stress acting on the crack. A procedure is outlined for the solution of a collection of interacting cracks in a series of time steps and for the computation of energy changes in the crack assembly during each time step. Elastodynamic effects are not considered. In spite of the simplicity of the proposed slip law, it is shown that complex material behaviour can occur if the model is applied in a random assembly of cracks. A particular demonstration is given of the simulation of primary, secondary and tertiary creep phases in a uniaxially compressed sample containing an initial population of weak flaws. The model is next applied to the simulation of face advance steps in a deep level gold mine excavation and is shown to give favourable agreement between observed seismic activity and the length of fractures mobilized in a random mesh of cracks around the opening. The modelled closure between the excavation roof and floor, as a function of time, is also shown to be quantitatively similar to the observed field movements. A final example is given of the mining of a parallel-sided excavation at different rates which illustrates the tradeoff between high face advance and high seismic activity and low face advance but potentially greater damage in the rock near the stope. © 1997 *Elsevier Science Ltd*

INTRODUCTION

The link between seismic activity and mining operations in deep level mines has been well established [1]. Elastic models of tabular mining operations have been used to delineate regions of potential seismic activity in terms of the implied stress drop on geological weaknesses near the edges of mine excavations [2,3]. Further extensions to this approach were proposed by Spottiswoode [4] in terms of the direct modelling of volumetric deformation processes around tabular excavations. More recently, Salamon [5] has stressed the necessity to quantify the relationship between mining activity and induced seismicity. Salamon [5] has proposed a novel procedure to establish this relationship by postulating the existence of populations of randomly disposed flaw sites surrounding the mine workings. The potential seismic stress drop on the flaws is calculated when the mine excavations are enlarged in progressive steps and Salamon's method provides a simulation tool to assess the expected seismic activity accompanying each mining step. Time-dependent constitutive effects are, however, not considered.

In hard rock mining, carried out in the sedimentary deposits of the South African gold fields, it is often found that both seismic activity and significant closure of the excavation surfaces can arise which is not associated only with changes to mining face positions. Time-dependent deformations have been observed over periods of hours, days or longer periods [6–8]. Seismic activity in highly stressed regions is found, also, to migrate spatially, presumably as a result of time-dependent fracturing and attendant stress transfer processes [9,10]. These effects have been highlighted in the case of rock mass preconditioning experiments where seismic activity moves away from a mining face that has been subjected to a preconditioning blast, towards adjacent areas that are more highly stressed [11]. The role of

†Division of Mining Technology, CSIR, P.O. Box 91230, Auckland Park, 2006, South Africa.

time-dependent deformation in relation to the stability of mine workings and the recurrence of seismic activity has been emphasized by Linkov [12]. In particular, Linkov has noted the importance of creep on discontinuity contacts. This time-dependent behaviour is highlighted also by investigators concerned with the modelling of earthquake phenomena [13–16].

In order to account for time-dependent seismic recurrence effects and to link these effects mechanistically to mining activity, it is necessary to represent in an explicit manner the rheological deformations that take place in the rockmass over periods of hours, days or weeks, as well as rapid elastodynamic excitations. This paper describes a framework for the incorporation of viscoplastic effects on random discontinuities which allows for the relaxation of the discontinuities according to a postulated law. Sudden stress drop or "elastodynamic" effects are approximated by allowing rapid cohesion loss (softening) to be accommodated in the solution scheme, but no attempt was made to include elastodynamic wave propagation effects in the current study. The most important aspect of the work is that explicit interaction between the mine openings and mobilized discontinuities is accounted for as an evolutionary time process. This allows realistic questions concerning practical mining problems to be addressed. Specifically, it becomes possible to investigate problems such as the consequences of varying the mining face advance rate, the effects of mining at greater depths, the desirability of continuous or punctuated mining cycles and questions relating to the rate of extraction of remnant areas and the expected recurrence of rockbursts and seismic energy release cycles.

A variety of discontinuity structures are present in the vicinity of deep level South African gold mines. These depend generally on the geological formation of the reef horizon that is extracted and may also be induced by blasting operations which form part of the mining cycle. In the case of sedimentary reef deposits, such as the Carbon Leader and Vaal Reef, it is often found that parting planes parallel to the reef horizon are readily mobilized by the mining operations [17]. In some cases the parting planes contain pre-existing gouge material which facilitates slip on the discontinuities [18]. It is also found that other gold bearing reefs, such as the Ventersdorp Contact reef, are overlain by lava deposits which contain multiple joint structures which show less propensity for movement. Pre-existing fault structures are also encountered which behave differently in response to stress changes induced by mining operations. In some cases fault exposures have been observed to be continually mobilized [10] but in other cases sudden slip occurs resulting in large scale damage to underground excavations. Little data are currently available to characterize the manifold properties of these discontinuities. Experimental work currently underway suggests that mining induced extension fractures and joints in lava may exhibit very long relaxation times, whereas discontinuities with gouge infilling may readily "creep" when shear loading is suddenly applied to the joint [18].

The approach presented in this paper sets out to explore the feasibility of modelling the viscoplastic behaviour of discontinuities by incorporating a simple time-dependent slip rule on explicit crack interfaces that are represented by small strain dislocations as embodied in the displacement discontinuity boundary integral method [19]. This approach facilitates the analysis of multiple interacting cracks such as joints, parting planes and faults which are characteristic of mining problems. It is demonstrated that realistic seismic energy release and stope closure trends can be simulated using a random mesh of potential discontinuity sites surrounding a tabular mining excavation. The justification for employing a random mesh representation is based on some success in modelling physical experiments of brittle rock failure [20], as well as the realistic replication of fracture patterns near mine openings [21]. In the present paper specific geological structures such as faults or parting planes are not considered. The approach used to estimate seismic energy release levels is described and the application of the model is illustrated by comparing simulated seismic energy release trends and stope closures to actual observations. The potential of the model to examine the effect of varying the mining face advance rate is illustrated. Although a simple time-dependent slip rule is used, it can easily be adapted within the developed framework to simulate behaviour appropriate to different discontinuity types.

VISCOPLASTIC DISPLACEMENT DISCONTINUITY MODEL FORMULATION

In previous work, carried out by Crawford and Curran [22], the displacement discontinuity method was employed in conjunction with the correspondence principle to analyse viscoelastic intact rock behaviour with inelastic joints or elastic intact rock with viscoelastic joints. Malan [8] also analysed time dependent stope closure using an analytical model of a tabular opening in a viscoelastic medium. In the present development, it is postulated that the intact rock material behaves in an essentially elastic manner and that all inelastic behaviour, including viscoplastic effects, is controlled by the presence of multiple interacting discontinuities. In this approach, explicit slip is modelled as a time-dependent (but not elastodynamic) process and progressive redistribution of stress can occur near the edges of mine openings both as a function of time and in response to changes to the size of the openings.

To make the analysis explicit, suppose that the problem region of interest is covered by a specified mesh of potential crack surfaces S_d and assume that each arc of the mesh is a straight line segment that is divided into one or more elements. It is assumed that the displacement vector may be discontinuous at any point

Q of the surface S_d. The displacement discontinuity vector $D_i(Q)$ at point Q is defined to be

$$D_i(Q) = u_i^-(Q) - u_i^+(Q) \tag{1}$$

where $u_i^-(Q)$ and $u_i^+(Q)$ represent the displacement vectors on the "negative" and "positive" sides of the surface S_d with respect to a defined normal $n_i(Q)$ at point Q. The displacement and stress influence of each element can be defined as described in Appendix A [19]. In the following development it is convenient to consider the stress values that arise at a given point within an element of length $2b$ which is centred on the y-axis of a local co-ordinate system y–z as shown in Fig. 1. In this system, the x-axis is assumed to be the direction of plane strain. Assuming that the displacement discontinuity varies linearly over the element of length $2b$ (Fig. 1), the local displacement discontinuity vector components can be expressed as

$$D_i(\eta) = \alpha_i + \beta_i \eta \tag{2}$$

where $i = y$ or z and α_i and β_i are constants.

The linear variation shape is more accurate than constant variation displacement discontinuities [22] and also allows direct estimates of crack-parallel stresses to be made without requiring numerical differentiation of adjacent element discontinuity values.

Let the shear and normal stress tractions at a designated collocation point, $y = c$, within a given element, be written in the form

$$\begin{bmatrix} T_y(c) \\ T_z(c) \end{bmatrix} = \frac{K_0}{b}\begin{bmatrix} D_y(c) \\ D_z(c) \end{bmatrix} + \frac{\bar{K}_0}{b}\begin{bmatrix} D_y(-c) \\ D_z(-c) \end{bmatrix} + \begin{bmatrix} E_y'(c) \\ E_z'(c) \end{bmatrix} \tag{3}$$

where E_y' and E_z' represent the total shear and normal stress tractions, at the designated point, due to primitive stresses and due to the stress induced by all other mobilized displacement discontinuity elements.

The values of K_0 and $\bar{K}_0$ depend on the collocation factor $c_f = c/b$ and can be deduced from equations (A5), (A6) and (A7) with $y = c$ and $z = 0$ (Appendix A).

$$K_0 = \frac{G}{4\pi(1-\nu)}\left[\frac{4}{1-c_f^2} + \frac{1}{2c_f}\log\left(\frac{1+c_f}{1-c_f}\right)^2\right] \tag{4}$$

$$\bar{K}_0 = -\frac{G}{4\pi(1-\nu)}\left[\frac{1}{2c_f}\log\left(\frac{1+c_f}{1-c_f}\right)^2\right]. \tag{5}$$

In cases of frictional sliding or creep relaxation,

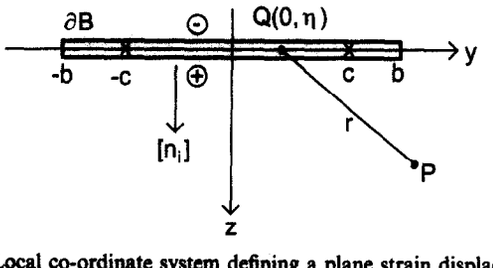

Fig. 1. Local co-ordinate system defining a plane strain displacement discontinuity element of length $2b$ and having two collocation points located at $y = \pm c$.

it is convenient to define the total external stress vector by

$$\begin{bmatrix} E_y(c) \\ E_z(c) \end{bmatrix} = \frac{\bar{K}_0}{b}\begin{bmatrix} D_y(-c) \\ D_z(-c) \end{bmatrix} + \begin{bmatrix} E_y'(c) \\ E_z'(c) \end{bmatrix}. \tag{6}$$

Substituting equation (6) into equation (3) and assuming implicit reference to a particular collocation point, equation (3) becomes

$$\begin{bmatrix} T_y \\ T_z \end{bmatrix} = \frac{K_0}{b}\begin{bmatrix} D_y \\ D_z \end{bmatrix} + \begin{bmatrix} E_y \\ E_z \end{bmatrix} \tag{7}$$

or

$$\mathbf{T} = (K_0/b)\mathbf{D} + \mathbf{E}. \tag{8}$$

Solution procedure

The determination of D_y and D_z will depend on the nature of the boundary condition imposed on each displacement discontinuity element. In this paper it is assumed that all elements are designated as "elastic" or "viscoplastic".

Let L designate the total set of defined elements. At each specific instance in time, t_i $(i = 1, 2, \ldots, N)$, M_i represents the set of mobilized elements and $\bar{M}_i$ is the complementary set of elements which have not been activated. Hence,

$$L = M_i \cup \bar{M}_i. \tag{9}$$

The set of active elements M_i arising at time t_i, will comprise a subset E_i of elastic elements and a subset V_i of viscoplastic elements. The classification of each element depends on the constitutive boundary conditions that are defined for the element as well as special rules which can be specified to control the transition of an element from "elastic" to "viscoplastic" status or vice versa. For example, a viscoplastic element may become elastic if it is subjected to a tensile stress component that causes the crack to open. E_i and V_i are non-intersecting sets and

$$M_i = E_i \cup V_i. \tag{10}$$

The complete solution to the problem is defined by the displacement discontinuity values that are associated with each element in the sequence of sets $M_1 \ldots M_N$ that arise at the designated times $t_1 \ldots t_N$, respectively. The displacement discontinuity values are determined in an evolutionary manner from time step to time step. At the start of time step i, elements are selected for mobilization from the set $\bar{M}_{i-1}$ by computing the stress values at each collocation point in each element. Assuming that compressive stresses are negative, the element will be selected for mobilization if the stress state $\mathbf{T}$ at either collocation point falls on or outside the bilinear Mohr–Coulomb envelope shown in Fig. 2.

In Fig. 2, S_0' and ϕ' designate the unmobilized values of the cohesion and friction angle, respectively, and S_0 and ϕ designate the residual mobilized values. T_c

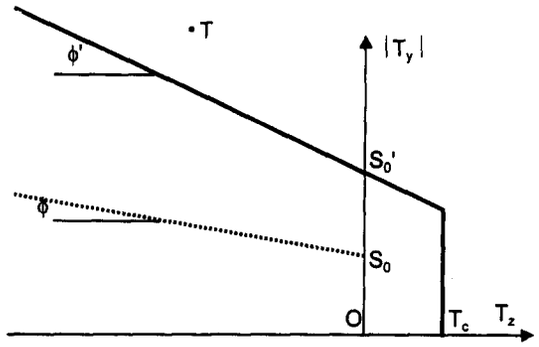

Fig. 2. Mohr–Coulomb diagram illustrating the selection of elements for mobilization.

designates the tensile strength of the element and is assumed to fall to zero if failure occurs.

The evolution of the solution proceeds in the following steps.

(i) At the start of time step i (time t_{i-1}) select all elements in $\bar{M}_{i-1}$ which can be mobilized. The selected elastic elements are designated as $\bar{E}_{i-1}$ and the selected viscoplastic elements are designated as $\bar{V}_{i-1}$

(ii) Form the provisional sets of elastic, $\hat{E}_i$, and viscoplastic, $\hat{V}_i$, elements for step i from the relations

$$\hat{E}_i = E_{i-1} \cup \bar{E}_{i-1} \tag{11}$$

$$\hat{V}_i = V_{i-1} \cup \bar{V}_{i-1} \tag{12}$$

(iii) Solve for the mutual interactions in set $\hat{E}_i$, using fixed external influences from the set $\hat{V}_i$, by iteratively adjusting the discontinuity values of $\hat{E}_i$.

(iv) Apply a viscoplastic relaxation step to adjust the discontinuity at every collocation point in the set of elements $\hat{V}_i$.

(v) Form the final sets E_i and V_i for time step i by checking for a change in status of each element in $\hat{E}_i$ and $\hat{V}_i$ which results from the adjusted displacement discontinuity values determined in steps (iii) and (iv).

(vi) Return to step (i) for the next time step.

The iterative solution in step (iii) proceeds by computing external stress values E_y, E_z at each collocation point and then accelerating these values. For simple Jacobi iteration, this procedure is as follows [23].

Let $E_y^{(k-1)}$ and $E_z^{(k-1)}$ represent external influences used in the $k-1^{st}$ iteration. Current estimates of $\hat{E}_y^{(k)}$ and $\hat{E}_z^{(k)}$ are determined from the discontinuity values existing at the end of the $k-1^{st}$ iteration. New estimates of $\hat{E}_y^{(k)}$ and $\hat{E}_z^{(k)}$ for the current step are determined from

$$\begin{bmatrix} E_y^{(k)} \\ E_z^{(k)} \end{bmatrix} = \begin{bmatrix} E_y^{(k-1)} \\ E_z^{(k-1)} \end{bmatrix} + \omega \begin{bmatrix} \hat{E}_y^{(k)} - E_y^{(k-1)} \\ \hat{E}_z^{(k)} - E_z^{(k-1)} \end{bmatrix} \tag{13}$$

where the multiplier ω is a defined relaxation factor. The residual error of the estimates is given by

$$\begin{bmatrix} r_y^{(k)} \\ r_z^{(k)} \end{bmatrix} = \begin{bmatrix} \hat{E}_y^{(k)} - E_y^{(k-1)} \\ \hat{E}_z^{(k)} - E_z^{(k-1)} \end{bmatrix}. \tag{14}$$

Current estimates of $D_y^{(k)}$ and $D_z^{(k)}$ are determined from specific boundary conditions imposed at the collocation point. For example, for an open crack or for the case of a tabular mine opening approximated as an open crack, tractions defined by equation (7) should be zero and therefore,

$$\begin{bmatrix} D_y^{(k)} \\ D_z^{(k)} \end{bmatrix} = -\frac{b}{K_0} \begin{bmatrix} E_y^{(k)} \\ E_z^{(k)} \end{bmatrix}. \tag{15}$$

Once a discontinuity is mobilized it is assumed that the tensile strength is zero. Hence, in the case of sliding friction contact it is required that

$$|T_y| = S_o - \tan\phi T_z; \quad T_z < 0. \tag{16}$$

Define a slip direction indicator, e, to be such that $e = 1$ if $E_y < 0$ and $e = -1$ if $E_y > 0$ then

$$|T_y| = -eT_y. \tag{17}$$

For a sliding crack it is assumed that the discontinuity opening displacement is given by

$$D_z = -\tan\psi |D_y| \tag{18}$$

where ψ is the sliding dilation angle, then the equilibrium condition (16) is satisfied if

$$D_y = \frac{-[E_y + e(S_o - \tan\phi E_z)]b}{K_0[1 + \tan\phi \tan\psi]}. \tag{19}$$

Other contact conditions, such as cohesion or friction weakening expressed as a function of slip D_y, or the inclusion of discontinuity stiffness values, can be treated using a similar formulation to that of equation (7) in which the collocation point self-effect and the external influence components of stress are decoupled and the external influence components are iterated as implied by equations (13) and (14). It is also possible to formulate more elaborate schemes to improve the iterative efficiency. This involves optimizing the choice of ω in each iteration step by successively approximating the nature of the residual error structure [23,24].

Viscoplastic relaxation and time step bounds

In order to resolve the viscoplastic relaxation step (iv) above, it is necessary to assume a specific functional dependence of the slip rate on the current stress state at each collocation point. Each slip element is assumed to be in quasi-static equilibrium at each instant in time, with the rate of slip being a function of the stress state and the resistance to slip. Specifically, define the resistance to slip, ρ, to be given by

$$\rho = S_o - \tan\phi T_z; \quad T_z < 0 \tag{20}$$

where S_o and ϕ are the residual cohesion and friction angle parameters as shown in Fig. 2. The "excess" driving shear stress, τ_e, is defined to be

$$\tau_e = |T_y| - \rho. \tag{21}$$

Using equations (7) and (17), equation (21) becomes

$$\tau_e = -e\left(\frac{K_0}{b} D_y + E_y\right) - (S_o - \tan\phi T_z). \quad (22)$$

From the definition of the slip direction indicator variable, e, the sign of the rate of change of slip, dD_y/dt is equal to e. It is now postulated that the rate of slip is proportional to the driving shear stress τ_e. Specifically,

$$\frac{dD_y}{dt} = e\kappa\tau_e \quad (23)$$

where κ is defined to be a parameter playing a similar role to the fluidity parameter of classical viscoplasticity theory [25]. This parameter will be designated as the surface fluidity having units of m/(Pa·sec). Substituting equation (22) into equation (23) and noting that $e^2 = 1$,

$$\frac{dD_y}{dt} = -\kappa\left[\frac{K_0}{b} D_y + E_y + e(S_o - \tan\phi T_z)\right]. \quad (24)$$

In discrete form,

$$D_y^{t_i} \approx D_y^{t_{i-1}} - \kappa\Delta t\left[\frac{K_0}{b} D_y^{t_{i-1}} + E_y + e(S_o - \tan\phi T_z)\right] \quad (25)$$

where

$$\Delta t = t_i - t_{i-1}. \quad (26)$$

The value of the confining stress T_z in equations (20) and (25) is assumed to be approximately constant over the time step Δt. The functional form of equation (24) is essentially equivalent to the relationship proposed by Wesson [26]. The cohesion S_o and friction angle ϕ can, in general, depend on the velocity dD_y/dt, the current slip D_y and time, t [15,26,27]. In the present study, S_o and ϕ are assumed to be constant. Equation (25) can be written in the more compact form

$$\Delta D_y^{t_{i-1}} = e\kappa\tau_e\Delta t. \quad (27)$$

Similarly, equation (19), with the dilation angle ψ set to zero, can be written for an incremental change in slip as

$$\Delta D_y = e\tau_e b/K_0. \quad (28)$$

Due to the discrete nature of the time step in equations (25) and (27) it is necessary that the magnitude of the change in equation (27) should be less than the maximum possible elastic slip relaxation given by (28). This implies a bound on the product of the time step Δt and the surface fluidity parameter κ such that

$$\kappa\Delta t < b/K_0. \quad (29)$$

This bound on the time step is analogous to the time step bound identified by Cormeau [28] for volumetric viscoplastic stress relaxation. It is clearly possible to extend the crude time stepping procedure given by equation (25) to a higher order Runge–Kutta scheme with automatic time step selection [29].

ESTIMATION OF SEISMIC ENERGY RELEASE

In the analysis of mining or earthquake problems it is convenient to define the gravitational body forces and far field tectonic forces as "loading" forces. In the course of mining or fault slip, the earth is deformed and the loading forces perform work. Let the incremental work done by the loading forces during a given time interval be ΔW_L. In the particular case of an elastic body, conservation of energy requires that

$$\Delta W_L = \Delta U + \Delta W_A \quad (30)$$

where ΔU is the change in internal strain energy and ΔW_A represents kinetic energy changes and energy dissipated by frictional sliding on discontinuities or consumed in creating new discontinuity surfaces. Consider in particular the transition between two states p and t which are associated with equilibrated stress and displacement fields $\tau_{ij}^p(Q)$, $u_i^p(Q)$ and $\tau_{ij}^t(Q)$, $u_i^t(Q)$, respectively, at each point Q of the body. In each case the body force field components $F_i(Q)$ remain the same. The work done by the loading force is shown in Appendix B to be given by

$$\Delta W_L = \Delta W_{Le} + \int_{S_d} [T_i^t(Q)D_i^p(Q) - T_i^p(Q)D_i^t(Q)]\, dS_Q \quad (31)$$

where

$$\Delta W_{Le} = \frac{1}{2}\int_{S_e} [T_i^t(Q) - T_i^p(Q)][u_i^t(Q) + u_i^p(Q)]\, dS_Q. \quad (32)$$

In equations (31) and (32), repeated subscripts imply summation over the requisite number of spatial components. S_d designates the internal discontinuity surfaces and S_e designates the external boundary surface of the body. $T_i^s(Q)$ represents, for time step s, the traction vector components at a given point Q of the internal or external surface with respect to a normal vector $n_i(Q)$ as defined in Appendix B. ΔW_{Le} represents the effect of the external surface S_e on the incremental work of the loading forces. In mining problems S_e can be considered to comprise both the earth's surface, where the tractions are zero, and a remote surface where the tractions are fixed ($T_i^t = T_i^p$) or where the displacement is zero. In this case ΔW_{Le} will be zero. The internal surface S_d can include narrow tabular openings which are approximated as cracks.

Equation (31) provides a means for computing the incremental loading work which accompanies a transition from state p to state t. The crucial assumption is now made that the equilibrated states p and t can be sufficiently well approximated using the static solution procedure outlined in the previous sections. Having identified two equilibrium states of the system, it is possible to compute the incremental work done by the

loading forces ΔW_L and the change in the strain energy ΔU. Since the two states p and t are computed using a quasi-static solution procedure, there will generally be an unaccounted gap ΔW_A between ΔW_L and ΔU. By conservation of energy, ΔW_A must be assumed to comprise both kinetic energy and other dissipated energy. ΔW_A can be loosely termed "released energy". If some estimate can be made of the energy that is dissipated by frictional sliding during the transition from state p to state t, it is possible to infer the maximum level of kinetic energy that could exist in the body during the transition. The kinetic energy is itself assumed to be dissipated by unspecified material damping and radiation mechanisms. The validity of this approximation rests on the assumption that elastodynamic stress waves do not give rise to significant additional fracture formation and that there is little "overshoot" in computing the final discontinuity values. The difference between ΔW_L and ΔU in equation (30) then provides a measure of the released energy which arises in the transition from state p to state t. This difference, ΔW_A, is shown in Appendix B to be given by

$$\Delta W_A = -\frac{1}{2}\int_{S_d} [T_i^t(Q) + T_i^p(Q)][D_i^t(Q) - D_i^p(Q)]\,dS_Q. \quad (33)$$

The level of kinetic or seismic energy, ΔW_S, that arises during the transition from state p to state t can be expressed as

$$\Delta W_S = \Delta W_A - \Delta W_D \quad (34)$$

where ΔW_D is the energy dissipated by frictional sliding or by the creation of new fracture surfaces. In the specific examples considered in this paper, it is assumed that in local discontinuity co-ordinates (Fig. 1) the dissipated energy is predominantly frictional and is given by

$$\Delta W_D = \int_{S_d} \tan\phi T_z(\eta)|D_y^t(\eta) - D_y^p(\eta)|\,d\eta \quad (35)$$

where T_z is the local stress component normal to the discontinuity surface S_d.

Equations (33) and (35) can be evaluated at each time step i by associating state p with the set of elements M_{i-1} mobilized at t_{i-1} and state t with the set of elements M_i mobilized at t_i. Approximate numerical values of (33) and (35) are obtained for each element by using the traction and displacement discontinuity vector components at the element collocation points in the following discrete sums.

$$\Delta W_A^{el} \approx -\frac{b}{2}\sum_{k=\pm 1} [T_i^p(kc) + T_i^t(kc)][D_i^t(kc) - D_i^p(kc)] \quad (36)$$

$$\Delta W_D^{el} \approx -\frac{b}{2}\tan\phi \sum_{k=\pm 1} T_z(kc)|D_y^t(kc) - D_y^p(kc)| \quad (37)$$

where kc is the collocation position in the local co-ordinate system defined in Fig. 1 and $T_z(kc) < 0$ for compressive stress normal to the element surface.

EXAMPLES AND APPLICATIONS

Strain softening and creep acceleration

It is of interest to consider first the viscoplastic response of an isolated straight crack in an infinite medium. Suppose that the crack lies on the y-axis of the local co-ordinate system shown in Fig. 1. The total shear traction T_y acting at position y within the crack is obtained by adding the induced shear stress $\tau_{yz}(y, 0)$ given by equation (A10), Appendix A, to the primitive far field shear stress component P_y. Specifically,

$$T_y(y) = \frac{G}{4\pi(1-\nu)}\int_{-b}^{b} \varphi_{,zz}(\eta, 0)D_y(\eta)\,d\eta + P_y \quad (38)$$

where $\varphi(y, z) = -\log[(y-\eta)^2 + z^2]$. The net driving shear stress, τ_e, acting on the crack is obtained by substituting equations (38), (20) and (17) into equation (21). This gives

$$\tau_e = -e\left\{\frac{G}{4\pi(1-\nu)}\int_{-b}^{b} \varphi_{,zz}(\eta, 0)D_y(\eta)\,d\eta + P_y\right\} - S_o + \tan\phi T_z. \quad (39)$$

The slip rate dD_y/dt at any point inside the crack is given by equation (23). When the crack has ceased to slip, $dD_y/dt = 0 = \tau_e$. The solution to equation (39) with $\tau_e = 0$ is given by [30],

$$D_y^*(\eta) = -\frac{2(1-\nu)}{G}[e(S_o - \tan\phi T_z) + P_y]\sqrt{b^2 - \eta^2}. \quad (40)$$

The slip motion on a single crack can be solved numerically, using the scheme corresponding to equation (25), for any particular choice of the surface fluidity parameter κ. Figure 3 shows the time evolution of the normalized maximum slip value at the centre of the crack when κ is set to 2×10^{-4} m/(MPa·day) and the crack is modelled using 20 equal length displacement discontinuity elements, with linear variation, described previously. The maximum slip values are scaled by the maximum asymptotic value $D_y^*(0)$ given by equation (40).

It is apparent that the simple slip law, represented by equation (23), predicts a monotonically decreasing rate of slip as the equilibrium condition $\tau_e = 0$ is approached. To replicate the behaviour of granular materials such as rock or concrete, suppose that a population of pre-existing flaws is represented as a random assembly of sliding cracks. If the initial flaw population is sufficiently dilute, then cohesionless cracks which are suitably oriented can be expected to have a response similar to that of the isolated crack shown in Fig. 3,

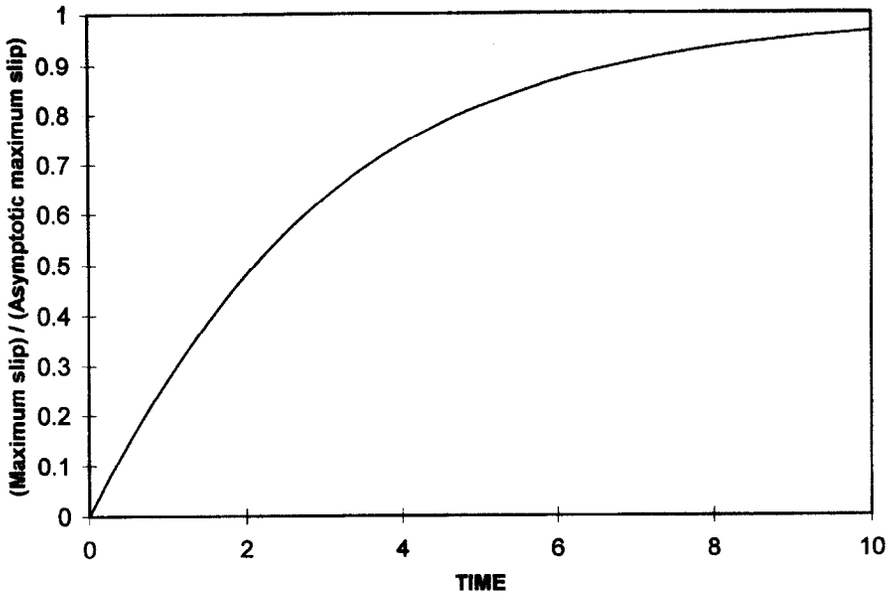

Fig. 3. Maximum slip evolution on a single crack.

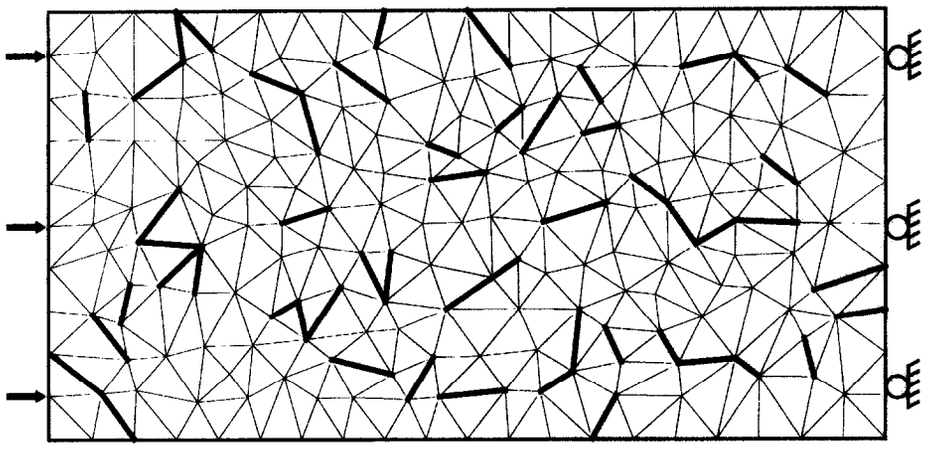

Fig. 4. Random population of sliding flaws. The highlighted flaws are assumed to have no cohesion or tensile strength.

when a load is suddenly applied to the material. The overall deformation of a sample of the material would be expected to follow primary creep behaviour [31] until sufficient slip on the mobilized flaws causes additional fracturing to occur. The progressive mobilization of fracturing may then result in a phase of secondary creep where the deformation is proportional to the loading time. As small fractures coalesce to form larger structures, it can be expected that accelerated deformation will occur leading eventually to a tertiary creep phase and collapse of the sample.

This sequence can, in fact, be reproduced by applying equation (23) to the random population of sliding flaws displayed in a rectangular region of width L and length $2L$ in Fig. 4. Approximately one tenth of the flaws, depicted by heavy lines in Fig. 4, are assumed to be "weak" and to have no cohesion or tensile strength. The remaining flaws are assumed to be "strong" and to have a uniform strength. Specific material properties of the weak and strong flaws are given in Table 1. The flaws in this case were generated using a Delaunay tessellation scheme [32] and the flaw size statistics are quoted in Table 1 relative to the dimension L of the sample. The flaw length frequency histogram is shown in Fig. 5.

It is now assumed that a load of 50 MPa (i.e. $2S_0'$) is applied to the left hand side of the sample and that the right hand side is rigidly restrained by a frictionless platen. It should be noted that the applied load is approximately 41% of the uniaxial strength corresponding to the material properties of the strong flaws (Table 1). The fluidity parameter κ is chosen to be

Table 1. Sample flaw population properties

Property	Weak flaws	Strong flaws
Cohesion, S_0' (MPa)	0	25
Friction, ϕ' (degrees)	30	45
Tensile strength, T_c (MPa)	0	10
Mobilized cohesion, S_0 (MPa)	0	0
Mobilized friction, ϕ (degrees)	30	30
Mean flaw length (normalized)	0.120	0.116
Standard deviation (normalized)	0.028	0.273
Minimum length (normalized)	0.072	0.070
Maximum length (normalized)	0.178	0.202
Total length (normalized)	6.352	55.75

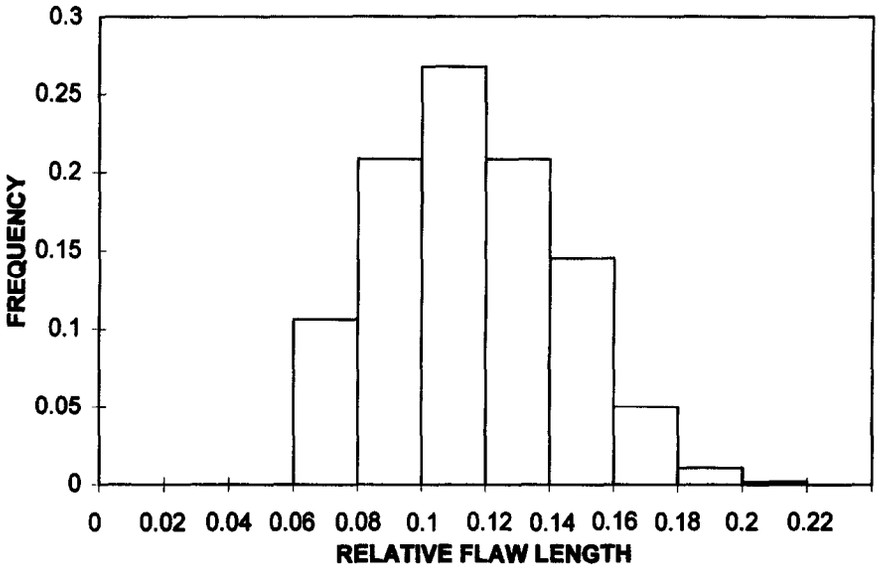

Fig. 5. Flaw size frequency distribution in rectangular sample loading test.

2×10^{-5} in an appropriate set of units and the time step size is set equal to 0.1 time units. The average strain component in the sample, parallel to the applied load, is shown as a function of time in Fig. 6 as well as the fraction of the total flaw length mobilized at each point in time. Before time 5, the strain increased at a decreasing rate which is similar to a primary creep phase. The length of mobilized flaws is also seen to increase slowly during this period. The duration of this period is governed by the weak flaw density and by the fluidity κ. Between time 5 and 14, the strain rate is observed to increase almost linearly with time, corresponding to an increased rate of mobilization of flaws. However, the rate of change of the flaw length falls off after time 10 indicating that the deformation occurs mainly by sliding on existing flaws between times 10 and 14. A sudden jump in the strain rate is observed between times 14 and 15, and this is followed by a generally accelerated deformation rate similar to a tertiary creep phase. The relatively abrupt increase in the strain rate between times 14 and 15 corresponds to an axial crack forming through the whole length of the sample as shown in Fig. 7. Accelerated flaw length mobilization is observed after time 17.

The example shown here demonstrates that plausible material behaviour can be simulated with a simple viscoplastic relaxation law. At the same time, the assumed material fabric, represented in this case by a random mesh of sliding cracks, plays a central role in controlling the overall strain response and the detailed damage mechanisms.

Application to deep level mining problems in brittle rock

The numerical framework outlined in this paper for the computation of time-dependent slip relaxation on multiple interacting discontinuities is particularly appropriate for the analysis of deep level gold mining problems in brittle rock. The following examples will

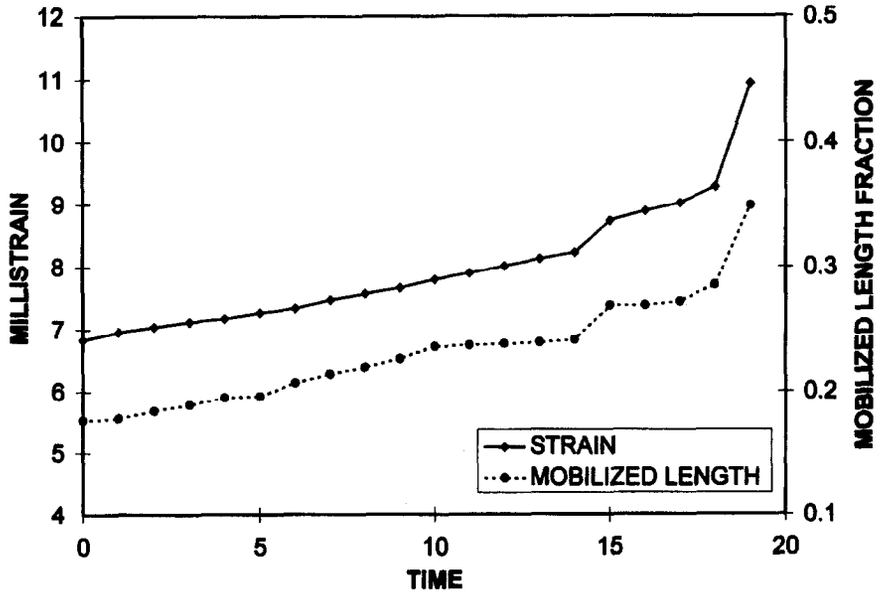

Fig. 6. Response of sample to sudden load.

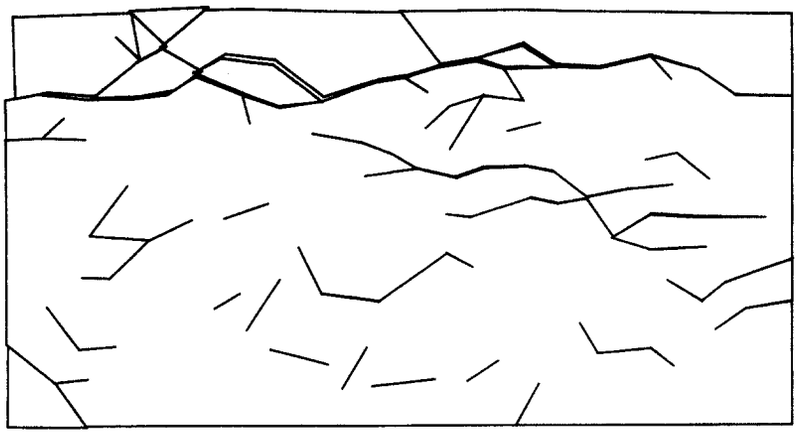

Fig. 7. Formation of axial crack parallel to the loading direction between times 14 and 15.

therefore concentrate on the mining of narrow tabular orebodies found in the South African gold mining industry. As mentioned in the Introduction, significant time-dependent rock behaviour has been noted in these mines by researchers monitoring seismic activity and closure behaviour. As a result of this viscous behaviour, rockbursts can occur some period after blasting when there is no external influence which could account for changes in stress distribution. A detailed investigation of time-dependent rock behaviour is therefore essential for a better understanding of deformation mechanisms and eventual improvement of safety in the mines.

In the South African mines the *in situ* time-dependent behaviour is much more significant than the creep behaviour of intact laboratory-sized specimens [33]. This was also noted by Kranz and Estey [34] who monitored the relaxation process in another deep hard rock mine. It is therefore generally accepted that the behaviour is governed mainly by the time-dependent migration of the fracture zone ahead of advancing faces [7]. If the fracture zone extension does not occur as fast as the rate of face advance, the stress peak will be shifted closer to the face increasing the possibility of strain bursting. Observational evidence of the time-dependent fracture process was obtained by Adams and Jager [35] who investigated the extent of the fracture zone that occurs ahead of advancing stope faces at the Doornfontein gold mine. They found the formation of fractures to be associated with the face advance where the majority of new fractures form within a relatively short period after blasting. The amount of new fracturing taking place then diminishes as the face stands. For a face that was not mined for a period of 14 days no new fractures could be observed. Further evidence of relaxation processes in the rock was obtained from seismic data. McGarr [36] investigated the dependence of magnitude statistics on aseismic rock deformation in the East Rand Proprietary Mines. It was found that the level of seismicity is determined by the rate of aseismic deformation. That is, the time-dependence of the seismicity is the result of aseismic deformation that occurs over an extended period. It appeared that the rock was undergoing logarithmic creep in response to stress changes due to either mine face advance or to seismic events. It was postulated that the aseismic deformation was due to progressive brittle failure as the rock temperature is too low to allow for continuum plastic deformation in the quartizites. Legge and Spottiswoode [37] investigated the spatial, temporal and energy related aspects of fracturing ahead of a stope face with reference to microseismic activity. Locations of microseismic events showed the region of primary fracturing located 5–10 m ahead of the faces. It was found that the total amount of seismic energy radiated during a typical face advance increment is a small portion of the total energy released on any individual day. Most energy is released in a stable manner by aseismic processes.

In order to simulate these processes with the numerical procedure developed above, the initial extraction of a tabular parallel sided panel is considered. The opening is approximated as a crack, with interpenetrating faces, embedded in a random mesh of potential discontinuity segments. The strength properties of each segment and the statistics of the random mesh are given in Table 2. Representative *in situ* rock properties were used with the surface fluidity κ determined by back-analysis of the measured underground time-dependent closure. The opening is created incrementally in a series of mining steps [38] and each segment of the random mesh is tested for failure at designated time step intervals. The seismic energy changes that occur in each time step are

Table 2. Properties of discontinuity strength and random mesh statistics used in the numerical simulations

Property	Mining simulation
Cohesion, S_0' (MPa)	25
Friction, ϕ' (degrees)	45
Tensile strength, T_c (MPa)	5
Mobilized cohesion, S_0 (MPa)	0
Mobilized friction, ϕ (degrees)	30
Mean segment length (m)	1.119
Standard deviation (m)	0.272
Minimum Segment length (m)	0.605
Maximum segment length (m)	2.073
Total length (m)	2594
Surface fluidity, κ, ($MPa^{-1}\cdot h^{-1}\cdot m$)	1×10^{-5}
Time step size, Δt (h)	0.1
Young's modulus (MPa)	70,000
Poisson's ratio	0.2
Vertical stress (MPa)	60 and 100
Horizontal stress (MPa)	30 and 100

computed using equations (34), (36) and (37) applied to each mobilized element. In this example, no geological features such as parting planes, parallel to the tabular opening, or faults are considered. The inclusion of these features is, however, accommodated directly by the solution procedure if necessary.

An important consequence of the numerical viscoplastic discontinuity behaviour is that the additional fracturing caused by a sudden increase in stress occurs in a time-dependent fashion. After a mining increment, the existing discontinuities surrounding the stope are subjected to an increase in mining induced stress. Those discontinuities subjected to stresses above the target yield surface, relax causing a transfer of stress to the solid rock at the edge of the fracture zone. New fractures then form in these positions as a time-dependent process. For the example above, the increase in cumulative fracture length as a function of time after a blast is illustrated in Fig. 8. It should be emphasized that there are no changes in the excavation dimension during this time period. Similarly to Adams and Jager's [35] observations, the majority of new fractures form within a short period after the blast and the rate of fracturing then diminishes until the next blast. For comparison with the numerical results, the cumulative seismicity after production blasting at an experimental site in the Blyvooruitzicht gold mine is also plotted in Fig. 8 [39]. A description of the site can be found in Kullmann *et al.* [40]. It is clear from Fig. 8 that a similar trend is observed for the seismicity. Events with magnitude greater than -1.5 were used. The seismicity following 304 production blasts was added, or stacked, for Fig. 8. All recorded events within 5 min of the start of the face blast were excluded because face blasting took approximately 5 min and most events within this time appeared to be face blasts.

In the numerical simulation, the time-dependent fracture process results in stope closure profiles similar to that observed underground. Typical numerical and experimental closure profiles measured after blasting ($t = 0$) are plotted in Fig. 9. The experimental closure data were also obtained form the experimental site at the Blyvooruitzicht Gold Mine. It should be emphasized that the purpose of the comparison in Fig. 9 is only to illustrate the similar trend in the numerical and experimental closure behaviour. Leeman [6] found that the rate of closure varied greatly from one point to the next and was affected by the position of the measuring point in relation to the support in the stope. This is caused by the discontinuous nature of the fracture zone. An exact fit between the numerical solution and experimental closure data at a particular point in the stope will therefore be meaningless.

Effect of mining rate

One strategy which may indeed be useful to control the stability of the fracture zone in the South African gold mining industry is the rate of stope face advance. A statistical analysis by Cook *et al.* [1] indicated an increase in rockbursts for a face advance rate of more than 4 m a month for small abutments and 8 m a month for large abutments. The mechanistic interpretation of these results was not investigated due to the lack of an appropriate constitutive representation of the time-dependent fracture zone processes in deep hard rock mines. As the viscoplastic discontinuity model developed above proved successful in simulating the observed time-dependent rock behaviour, it was subsequently used to investigate the effect of mining rate on seismic energy release.

A series of mining advance rates was analysed for a parallel-sided stope panel by specifying different numbers of time steps between each mining step. Figure 10(a) shows a cumulative plot of seismic energy released as a function of the mined length for three different face advance rates of 2 m/day, 1 m/day and

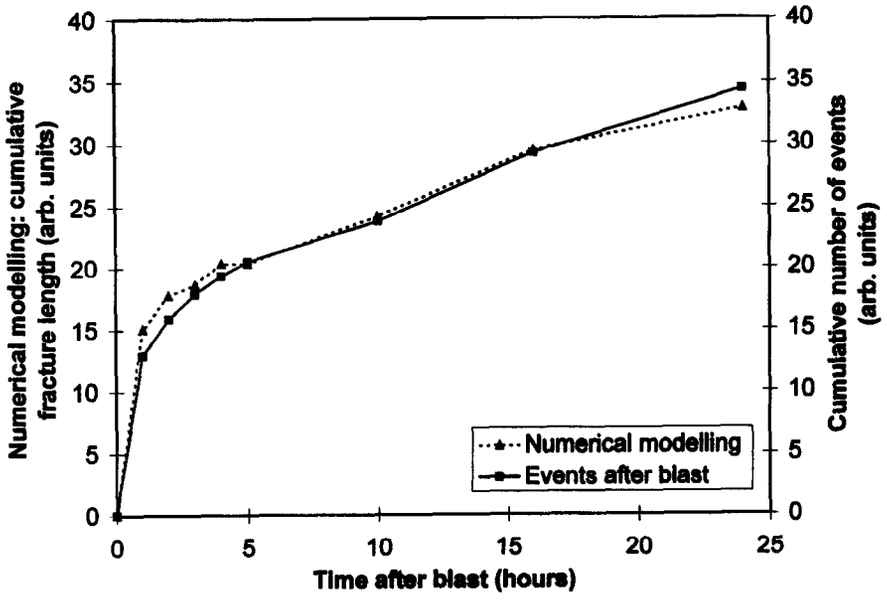

Fig. 8. Cumulative fracture length after blasting. The rate of seismicity after blasts are also plotted showing similar trends.

Table 1. General characteristics of the sites [3]

Site No.	Method F.I. or H.F.	Gallery	Depth (m)	Elevation seam (m)	Bedding: Line of maximum slope dip (°)	Bedding: Line of maximum slope azimuth	Number of useful tests	Date
1	F.J.	T.B. 90	390	60	6	N 305	8	Nov. 1980
2	F.J.	T.B. 90	390	150	7	N 000	5	Dec. 1980
3	F.J.	T.B. 33	700	− 10	9	N 270	6	Nov. 1979
4	F.J.	T.B. 235	550	50	9	N 250	10	May 1980
5	H.J.	roadway 25 Etoile	700	− 10 − 25	7	N 245	0	May 1986
6	H.F.	roadway 75b Etoile sud	900	− 10 − 25	10	N 300	6	June 1986
7	H.F.	roadway 83 Estaque nord	1030	− 15 − 30	10	N 280	5	Apr. 1987
8	H.F.	roadway 19 Eguilles	1140	− 13 − 25	9	N 280	4	Nov. 1990
9	H.F.	roadway 59 Estaque sud	1200	− 10 − 28	17	N 292	6	June 1992
10	H.F.	intersect 60–59 Estaque sud	1130	− 12 − 34	16	N 283	6	Oct. 1992
11	H.F.	Arbois	1260	− 10 − 28	7	N 280	4	Nov. 1993

F.J.: flat jack; H.F.: hydraulic fracturing.

Table 2 summarises the magnitudes and orientations of the principal stresses measured at each site [3]. The vertical stress is significantly smaller than the theoretical value calculated on the basis of the weight of overburden. Moreover, the ratio between the vertical stress (σ_V) and the weight of overburden ranges from 0.40 to 0.87. The stress measurements show that the major principal stress (σ_1) is always horizontal and corresponds to the maximum horizontal stress. The stress σ_1 is two–four times larger than the minor principal stress (σ_3) which is almost equal to the minimum horizontal stress, whereas the intermediate principal stress is vertical ($\sigma_V = \sigma_2$) except for sites 6 and 8.

From these measurements, a strong stress anisotropy and high stress level were also observed, and two distinct stress areas can be distinguished: one regrouping sites 7, 8, 10 and 11 corresponding to a horizontal compression which is clearly anisotropic with an east–west towards north east–south west direction (this direction remains identical to those found in the other sites located more eastward: 3 and 4) and the other regrouping sites 6 and 9 for which the stress state is approximately isotropic [3]. Especially for site 9, the major, minor and intermediate principal stress values are respectively 22, 18 and 20 MPa; the major principal stress direction (N170°E) is close to that of the north–south regional compression.

Generally speaking, the principal stress magnitudes and orientations vary non-uniformly from one site to another. It should be noted that the stress heterogeneities are characteristic of the sedimentary series due to differences in the mechanical characteristics from one bed to another [7–9]. Except for site 9, the orientation of the major principal stress (σ_1) varies between N40°E and N104°E.

3. NUMERICAL MODELLING

Numerical modelling is of great importance in geology for understanding displacement, stress and strain phenomena, and even fault formation [10–17]. The numerical models used are large scale models, based on between 10 and several hundred kilometres.

The modelling that we undertake must be viewed in this general framework. It consists of explaining the stress distribution in the Arc syncline.

Table 2. Natural stresses obtained from *in situ* measurements [3]

Site no.	Magnitude σ_1	Magnitude σ_2	Magnitude σ_3	Direction σ_1	Direction σ_2	Direction σ_3	Ratio σ_V/γ^*h
1	8	8	7	N 135	V	N 45	0.82
2	6.5	6.5	3	N 135	V	N 45	0.64
3	16	7	2.5	N 115	V	N 25	0.39
4	19	10	5	N 60	V	N 150	0.71
6	40	17	12	N 150	N 60	V	0.53
7	32	19	16	N 70	V	N 160	0.73
8	31	23	20	N 104	N 14	V	0.80
9	22	20	18	N 170	V	N 80	0.67
10	45	20	15	N 40	V	N 130	0.71
11	34	27.5	20	N 100	V	N 10	0.87

V: vertical direction; γ^*h: the theoretical stress calculated (where $\gamma = 0.025$ MN/m^3 is the unit weight of the rock and h is the depth beneath the surface).

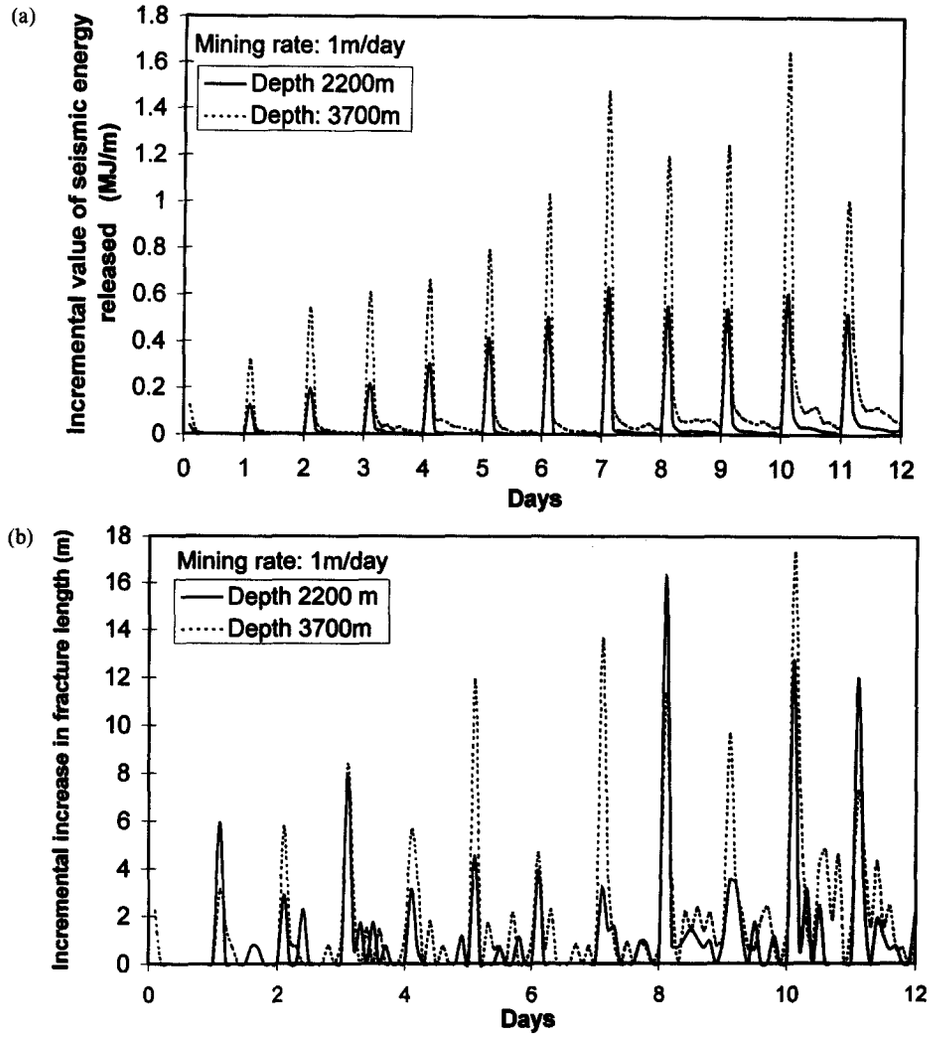

Fig. 11. (a) Incremental seismic energy release. (b) Incremental mobilized fracture length.

1 m/2 days. The nominal mining depth is 2200 m with a vertical primitive stress of 60 MPa at the mining horizon. The horizontal primitive stress is assumed to be 30 MPa at this position. To help the reader estimate typical runtimes, the 2 m/day solution took nearly 5 h on a 200 MHz Pentium computer. Up to a face advance of 16 m there appears to be little difference in the seismic energy release in each case. After this point, the highest mining rate (2 m/day) is seen to release significantly more energy. At the same time it is of great interest to examine the cumulative length of mobilized fractures shown in Fig. 10(b). Here, it is apparent that at mining distances greater than 14 m, more fractures are mobilized at the slower mining rate. Significantly, it can be seen that when the mining has advanced to 28 m, approximately 20% more fractures are mobilized if the slowest rate of 1 m/2 days is pursued as compared to the mining rate of 1 m/day, although, from Fig. 10(a), there is little difference in the cumulative released energy. This illustrates the important point that while slow mining may lead to a smaller cumulative release of seismic energy, more damage or slip movements may arise in the rockmass which in turn may lead to local support difficulties in terms of rock falls and shake out.

Figure 11(a) shows the incremental seismic energy release within each time step as mining proceeds at an advance rate of 1 m/day. The release pattern is contrasted for two mining depths of nominally 2200 m (60 MPa) and 3700 m (100 MPa), respectively. Figure 11(a) shows clearly that most seismic energy is released immediately after each sudden advance of the mining face. Additional seismic activity is seen to occur at a generally decreasing rate before the next face advance step. This corresponds qualitatively to the very well known pattern of seismic activity that is observed in deep level gold mines between each blast cycle [1]. Figure 11(a) also indicates that greater levels of seismic activity occur at the greater depth. In some cases, secondary peaks can be observed between face advance cycles. It is also of interest to note that following an initial trend of increasing energy release peaks in the first seven days, successive peak values become more random. The corresponding mobilized fracture length in each time step is shown in Fig. 11(b) for the two mining depths. The successive peak values are more irregular than the energy release peaks. It can be seen from Fig. 11(b) that more fractures are mobilized at the increased depth. More extensive simulation studies are required to determine the fracture extent for a wide

span stope once total closure of the mined region occurs.

CONCLUSIONS

A framework has been presented for the solution of interacting crack assemblies in which a discontinuum viscoplastic formation is used to control the rate of slip on individual cracks. It is shown that this approach is able to reproduce intricate material behaviour such as primary, secondary and tertiary creep effects when the rock fabric is represented by a set of interacting cracks which are specified on a random mesh. When applied to mining problems, favourable agreement is found between observed numbers of seismic events following actual face advances and the cumulative length of fractures that are mobilized in a simulated stope panel embedded in a random mesh of discontinuities. In addition, the numerically computed time-dependent closure, at a given point in the stope panel, follows the same qualitative trend as the actual observations of the stope closure.

The computation of strain energy release in a population of interacting discontinuities is described and is determined as a function of time for a parallel-sided mine panel which is enlarged at three different rates. This demonstrates that a balance must be struck between higher energy release rates (potentially damaging rockbursts) at high face advance rates and greater deformation of the rockmass, with greater potential for local rockfalls, at slower mining rates.

In general, it is suggested that the analysis procedure described in the paper provides a useful framework for the explicit mechanistic representation of time dependent seismic diffusion and stress transfer processes that are observed in deep level mines. The basis for the approach depends on the specification of potentially active cracks in the rockmass which are, for convenience, disposed on the arcs of a random mesh. This structure can, however, be readily adapted to include discontinuities which are aligned with known lineations in the rockmass such as joint sets or bedding and parting planes, and to represent geological structures such as faults or dykes. The solution method outlined in the paper is based on the use of small strain displacement discontinuities, although any numerical procedure capable of analysing large scale interacting discontinuities can be used for this purpose. However, an important challenge is to consider the extension of the method to three dimensions for the effective analysis of regional mine layout problems.

Acknowledgements—This work forms part of the rockmass behaviour research programme of Rock Engineering, CSIR Division of Mining Technology. The authors acknowledge the financial assistance and support received from the Safety in Mines Research Advisory Committee (SIMRAC). D. F. Malan is working towards a Ph.D degree at the University of the Witwatersrand and some of the work described here also forms part of that study. We wish to express our thanks to Prof. A. M. Linkov, Prof. J. A. Hudson and an anonymous referee for improving the quality of the paper with their helpful comments.

Accepted for publication 9 June 1997

REFERENCES

1. Cook, N. G. W., Hoek, E., Pretorius, J. P. G., Ortlepp, W. D. and Salamon, M. D. G., Rock Mechanics applied to the study of rockbursts. *J. S. Afr. Inst. Min. Metall.*, 1966, **66**, 435–528.
2. Ryder, J. A., Excess shear stress in the assessment of geological hazardous situations. *J. S. Afr. Inst. Min. Metall.*, 1988, **88**, 27–39.
3. Spottiswoode, S. M., Towards 3D modelling of inelastic deformation around deep-level mines. In *Proc. Int. Conf. Mechanics of Jointed and Faulted Rock*, ed. H. P. Rossmanith, Balkema, pp. 695–707, 1990.
4. Spottiswoode, S. M., Volume of excess shear stress and cumulative seismic moments. In *Proc. 2nd Int. Symp. Rockbursts and Seismicity in Mines*, ed. C. Fairhurst, Balkema, pp. 39–43, 1990.
5. Salamon, M. D. G., Keynote address: Some applications of geomechanical modelling in rockburst and related research. In *Proc. 3rd Int. Symp. Rockbursts and Seismicity in Mines*, ed. R. P. Young, Balkema, pp. 297–309, 1993.
6. Leeman, E. R., Some measurements of closure and ride in a stope of the East Rand Proprietary Mines. *Pap. Ass. Min. Mngrs. S. Afr.* 1958, **1958–1959**, 385–404.
7. McGarr, A. Stable deformation near deep-level tabular excavations. *J. Geophys. Res.*, 1971, **76**, 7088–7106.
8. Malan, D. F., A viscoelastic approach to the modelling of the transient closure behaviour of tabular excavations after blasting. *J. S. Afr. Inst. Min. Metall.*, 1995, **95**, 211–220.
9. Mendecki, A. J., Real time quantitative seismology in mines. Keynote Lecture. In *Proc. 3rd Int. Symp. Rockbursts and Seismicity in Mines*, ed. R. P. Young, Balkema, pp. 287–295, 1993.
10. Van Aswegen, G. and Butler, A. G., Applications of quantitative seismology in South African gold mines. In *Rockbursts and Seismicity in Mines*, ed. R. P. Young, Balkema, pp. 261–266, 1993.
11. Lightfoot, N., Goldbach, O. D., Kullmann, D. H. and Toper, A. Z., Rockburst control in the South African deep level gold mining industry. In *Rock Mechanics Tools and Techniques, Proc. 2nd North American Rock Mechanics Symposium: NARMS'96*, ed. M. Aubertin, F. Hassani and H. Mitri, pp. 295–303, 1996.
12. Linkov, A. M., Keynote address: Equilibrium and stability of rock masses. In *Proc. 8th Int. Congress on Rock Mechanics*, ed. T. Fujii, Vol. III, Japan, Balkema, 1995.
13. Scholz, C. H., Wyss, M. and Smith, S. W., Seismic and aseismic slip on the San Andreas Fault. *J. Geophys. Res.*, 1969, **74**, 2049–2069.
14. Lehner, F. K., Li, V. C. and Rice, J. R. Stress diffusion along rupturing plate boundaries. *J. Geophys. Res.*, 1981, **86**, 6155–6169.
15. Rice, J. R., The mechanics of earthquake rupture. In *Physics of the Earth's Interior*, ed. A. M. Dziewonski and E. Boschi, Italian Physical Society, Bologna, Italy, pp. 555–649, 1980.
16. Ben-Zion, Y. and Rice, J. R., Earthquake failure sequences along a cellular fault zone in a three-dimensional elastic solid containing asperity and nonasperity regions. *J. Geophys. Res.*, 1993, **98**, 14,109–14,131.
17. King, R. G., Jager, A. J., Roberts, M. K. C. and Turner, P. A., Rock mechanics aspects of stoping without back-area support. Unpublished COMRO (Chamber of Mines Research Organization, now CSIR Miningtek) research report, no. 17/89, 1989.
18. Malan, D. F., Drescher, K. and Vogler, U. W., Shear creep of discontinuities in hard rock surrounding deep level excavations. Submitted to *Proceedings Third International Conference on Mechanics of Jointed and Faulted Rock*, ed. H. P. Rossmanith, Vienna, 1998.
19. Crouch, S. L. and Starfield, A. M., *Boundary Element Methods in Solid Mechanics*. 1st edn. George Allen & Unwin, London, 1983.
20. Napier, J. A. L. and Dede, T., A comparison between random mesh schemes and explicit growth rules for rock fracture simulation. Accepted for publication in *Proc. 36th US Symp. Rock Mech.*, New York, 1997.
21. Sellers, E., A tessellation approach for the simulation of the fracture zone around a stope. Submitted to *Proceedings 1st Southern African Rock Engineering Symposium*, Johannesburg, 1997.

22. Crawford, A. M. and Curran, J. H., A displacement discontinuity approach to modelling the creep behaviour of rock and its discontinuities. *Int. J. Num. Anal. Meth. Geomech.*, 1983, 245–268.
23. Ryder, J. A., Optimal iteration schemes suitable for general non-linear boundary element modelling applications. In *Computer Methods and Advances in Geomechanics*, ed. Beer, Booker and Carter, pp. 1079–1084, 1991.
24. Peirce, A., Optimal iteration of discretized boundary element equations, CSIR, Division of Mining Technology project report, 1993.
25. Perzyna, P., Fundamental problems in viscoplasticity. *Adv. Appl. Mech.*, 1966, **9**, 243–377.
26. Wesson, R. L., Dynamics of fault creep. *J. Geophys. Res.*, 1988, **93**, 8929–8951.
27. Ruina, A., Slip instability and state variable friction laws. *J. Geophys. Res.*, 1983, **88**, 10,359–10,370.
28. Cormeau, I., Numerical stability in quasi-static elasto/visco-plasticity. *Int. J. Num. Methods Eng.*, 1975, **9**, 109–127.
29. Press, W. H., Flannery, B. P., Teukolsky, S. A. and Vetterling, W. T., *Numerical Recipes*, Cambridge University Press, 1986.
30. Sneddon, I. N. and Lowengrub, M., *Crack Problems in the Classical Theory of Elasticity*, John Wiley, New York, 1969.
31. Dusseault, M. B. and Fordham, C. J., Time-dependent behavior of rocks. In *Comprehensive Rock Engineering*, ed. J. A. Hudson, Vol. 3, Pergamon Press, pp. 119–149, 1993.
32. Tsai, V. J. D., Fast topological construction of delaunay triangulations and voronoi diagrams. *Computers and Geosciences*, 1993, **19**, 1463–1474.
33. Malan, D. F., Vogler, U. W. and Drescher, K., Time-dependent behaviour of hard rock in deep level gold mines. *J. S. Afr. Inst. Min. Metall.*, 1997, **97**, 135–147.
34. Kranz, R. L. and Estey, L. H., Listening to a mine relax for over a year at 10 to 1000 meter scale. In *Proc. 2nd North Am. Rock Mech. Symp:* NARMS '96, ed. M. Aubertin, F., Hassani and H. Mitri, Montreal, pp. 491–498, 1996.
35. Adams, G. R. and Jager, A. J., Petroscopic observations of rock fracturing ahead of stope faces in deep-level gold mines. *J. S. Afr. Inst. Min. Metall.*, 1980, **44**, 204–209.
36. McGarr, A., Dependence of magnitude statistics on strain rate. *Bull. Seism. Soc., Am.*, 1976, **66**, 33–44.
37. Legge, N. B. and Spottiswoode, S. M., Fracturing and microseismicity ahead of a deep gold mine stope in the pre-remnant and remnant stages of mining. In *ISRM 6th Int. Congr. Rock Mech.*, Montreal, pp. 1071–1077, 1987.
38. Crouch, S. L., Computer simulation of mining in faulted ground. *J. S. Afr. Inst. Min. Metall.*, 1979, **79**, 159–173.
39. Malan, D. F. and Spottiswoode, S. M., Time-dependent fracture zone behaviour and seismicity surrounding deep level stoping operations. Accepted for publication in *Proc 4th Int. Symp. Rockbursts & Seismicity in Mines*, ed. S. J. Gibowicz, Krakow, Poland, Balkema, 1997.
40. Kullman, D. H., Stewart, R. D. and Grodner, M., A pillar preconditioning experiment on a deep-level South African gold mine. In *Proc. 2nd North Am. Rock Mech. Symp:* NARMS '96, ed. M. Aubertin, F. Hassani and H. Mitri, Montreal, pp. 375–380, 1996.
41. Peirce, A. P. and Napier, J. A. L., A spectral multipole method for efficient solution of large-scale boundary element models in elastostatics. *Int. J. Num. Methods Eng.*, 1995, **38**, 4009–4034.
42. Napier, J. A. L., Energy changes in a rockmass containing multiple discontinuities. *J. S. Afr. Inst. Min. Metall.*, 1991, **91**, 145–157.
43. Salamon, M. D. G., Energy considerations in rock mechanics: Fundamental results. *J. S. Afr. Inst. Min. Metall.*, 1984, **84**, 223–246.
44. Sokolnikof, I. S., *Mathematical Theory of Elasticity*, McGraw-Hill, New York, 1956.
45. Salamon, M. D. G., Rock mechanics of underground excavations. *Proc. 3rd Cong. International Society for Rock Mechanics*, pp. 951–1099, 1974.

APPENDIX A

Let $u_i(y, z)$ and $\tau_{ij}(y, z)$ designate the components of the displacement vector and the stress tensor, respectively, at point $P(y, z)$ due to a single displacement discontinuity element located between $y = -b$ and $y = b$ of the local y–z co-ordinate system shown in Fig. 1.

Let the displacement discontinuity vector have components $D_i(\eta)$ at point $Q(\eta, 0)$ within the element. For a n^{th} order polynomial variation of the components $D_i(\eta)$ assume that

$$D_i(\eta) = \sum_{k=0}^{n} a_{ik}\eta^k \tag{A1}$$

where $i = y$ or z and a_{ik} are constants. Define the k^{th} order harmonic potential integral $I_k(y, z)$ as

$$I_k(y, z) = \int_{-b}^{b} \varphi\eta^k \, d\eta \tag{A2}$$

where

$$\varphi = -\log[(y - \eta)^2 + z^2]. \tag{A3}$$

Generalizing the results of Crouch and Starfield [19], it can be shown that the displacement vector components at $P(y, z)$ are given by

$$\begin{bmatrix} u_y(y, z) \\ u_z(y, z) \end{bmatrix} =$$

$$\frac{1}{8\pi(1-\nu)} \sum_{k=0}^{n} \begin{bmatrix} 2(1-\nu)I_{k,z} + zI_{k,zz} & -(1-2\nu)I_{k,y} - zI_{k,yz} \\ (1-2\nu)I_{k,y} - zI_{k,yz} & 2(1-\nu)I_{k,z} - zI_{k,zz} \end{bmatrix} \begin{bmatrix} a_{yk} \\ a_{zk} \end{bmatrix} \tag{A4}$$

where $I_{k,y}$ designates $\partial I_k/\partial y$, etc. and ν is the Poisson's ratio of the material. The components of the stress tensor are given by

$$\begin{bmatrix} \tau_{yy}(y, z) \\ \tau_{yz}(y, z) \\ \tau_{zz}(y, z) \end{bmatrix} = \frac{G}{4\pi(1-\nu)} \sum_{k=0}^{n} \begin{bmatrix} 2I_{k,yz} + zI_{k,yyz} & I_{k,zz} + zI_{k,zzz} \\ I_{k,zz} + zI_{k,zzz} & -zI_{k,yzz} \\ -zI_{k,yzz} & I_{k,zz} - zI_{k,zzz} \end{bmatrix} \begin{bmatrix} a_{yk} \\ a_{zk} \end{bmatrix} \tag{A5}$$

where G is the shear modulus of the material. In the case of linear variation elements, $n = 1$, and the required harmonic potential integrals defined by equation (A2) are as follows.

$$I_0(y, z) = \int_{-b}^{b} \varphi \, d\eta = \sum_{\epsilon=-1,1} \epsilon[B \log R^2 - 2B - 2z \tan^{-1}(z/B)] \tag{A6}$$

and

$$I_1(y, z) = \int_{-b}^{b} \varphi\eta \, d\eta = \sum_{\epsilon=-1,1} \epsilon[(yB - \tfrac{1}{2}R^2)\log R^2 - 2yB + \tfrac{1}{2}B^2 - 2yz \tan^{-1}(z/B)] \tag{A7}$$

where $\epsilon = -1$ and $+1$; $B = y - \epsilon b$ and $R^2 = B^2 + z^2$.

When $n = 1$, the coefficients in equation (A1) can be determined from

$$a_{i0} = \tfrac{1}{2}[D_i(c) + D_i(-c)] \tag{A8}$$

$$a_{i1} = \frac{1}{2c}[D_i(c) - D_i(-c)] \tag{A9}$$

where c is a chosen collocation position within the displacement discontinuity element. The total stress at point $P(y, z)$ is obtained by adding the primitive field stress to the stress tensor components, calculated using equations (A5). For a general variation of the discontinuity density components $D_i(\eta)$, the second member of equation (A5) can be written for the particular case $z = 0$, in the following form

$$\tau_{iz}(y, 0) = \frac{G}{4\pi(1-\nu)} \int_{-b}^{b} \varphi_{,zz}(\eta, 0) D_i(\eta) \, d\eta. \tag{A10}$$

APPENDIX B

Consider a body of volume V with external surface S_e and containing internal discontinuities or cuts which are defined by adjacent surfaces

S_d^+ and S_d^- occupying the same spatial positions initially of a common surface S_d [42]. The overall surface of the body, S, is therefore defined to be

$$S = S_e + S_d^+ + S_d^-. \tag{B1}$$

The plus and minus superscripts are defined with respect to an assigned normal to the surface S_d having components n_i. The components of the outward normals to the surfaces S_d^+ and S_d^- are therefore given by

$$n_i^+ = -n_i \tag{B2}$$

and

$$n_i^- = n_i. \tag{B3}$$

Consider the transition between two states p and t which are associated with equilibrated stress and displacement fields $\tau_{ij}^p(Q), u_i^p(Q)$ and $\tau_{ij}^t(Q), u_i^t(Q)$, respectively, at each point Q of the body. In each case the body force field components $F_i(Q)$ remain the same. Define ΔW_L to be the incremental work done by the loading forces $F_i(Q)$ and by tractions which change from T_i^p to T_i^t on the external surface S_e. Then

$$\Delta W_L = \int_V F_i(Q)\Delta u_i(Q)\,dV_Q + \frac{1}{2}\int_{S_e} [T_i^p(Q) + T_i^t(Q)]\Delta U_i(Q)\,dS_Q \tag{B4}$$

where V designates the volume of the body, and where

$$\Delta u_i(Q) = u_i^t(Q) - u_i^p(Q) \tag{B5}$$

The volume integral over V in equation (B6) can be expressed in terms of surface integrals, by applying the reciprocal work theorem to the equilibrated state F_i, τ_{ij}^p, u_i^p and the incremental state $\Delta\tau_{ij}$, Δu_i [43]. This results in the expression

$$\int_V F_i(Q)\Delta u_i(Q)\,dV_Q = \int_{S_e} [\Delta T_i(Q)u_i^p(Q) - T_i^p(Q)\Delta u_i(Q)]\,dS_Q + \int_{S_d} [\Delta T_i(Q)D_i^p(Q) - T_i^p(Q)\Delta D_i(Q)]\,dS_Q \tag{B6}$$

where

$$\Delta T_i(Q) = T_i^t(Q) - T_i^p(Q) \tag{B7}$$

and where

$$D_i(Q) = U_i^-(Q) - U_i^+(Q) \tag{B8}$$

as defined by equation (1). The integral over the discontinuity surface S_d is resolved using equations (B2) and (B3). For example,

$$\int_{S_d^+ + S_d^-} \Delta T_i(Q)u_i(Q)\,dS_Q = \int_{S_d^+} \Delta\tau_{ij}^+(Q)n_j^+(Q)u_i^+(Q)\,dS_Q + \int_{S_d^-} \Delta\tau_{ij}^-(Q)n_j^-(Q)u_i^-(Q)\,dS_Q = \int_{S_d} \Delta T_i(Q)D_i(Q)\,dS_Q.$$

Substituting equation (B6) into (B4) yields

$$\Delta W_L = \Delta W_{Le} + \int_{S_d} [T_i^t(Q)D_i^p(Q) - T_i^p(Q)D_i^t(Q)]\,dS_Q \tag{B9}$$

where

$$\Delta W_{Le} = \frac{1}{2}\int_{S_e} [T_i^t(Q) - T_i^p(Q)][u_i^p(Q) + u_i^t(Q)]\,dS_Q. \tag{B10}$$

ΔW_{Le} represents the effect of the external surface S_e on the incremental work of the loading forces. In mining problems S_e can be considered to comprise both the earth's surface, where the tractions are zero, and a remote surface where the tractions are fixed ($T_i^t = T_i^p$) or where the displacement is zero. In this case ΔW_{Le} will be zero. Since the p and t states are assumed to be equilibrated, the change in strain energy ΔU can be determined from Clapeyron's theorem [44,45]. Using the surface partition defined by equation (B1) and employing equation (B6) to eliminate the work done by the body forces, Clapeyron's theorem yields

$$\Delta U = \Delta W_{Le} + \frac{1}{2}\int_{S_d} [T_i^t(Q) - T_i^p(Q)]\,[D_i^p(Q) + D_i^t(Q)]\,dS_Q. \tag{B11}$$

The kinetic and dissipated energy ΔW_A is equal to

$$\Delta W_A = \Delta W_L - \Delta U. \tag{B12}$$

Substituting equations (B4) and (B11) into equation (B12), it is possible to express ΔW_A as follows

$$\Delta W_A = -\frac{1}{2}\int_{S_d} [T_i^t(Q) + T_i^p(Q)][D_i^t(Q) - D_i^p(Q)]\,dS_Q. \tag{B13}$$